Effects of atom numbers on the miscibility-immiscibility transition of a binary Bose-Einstein condensate

Lin Wen,[1] Hui Guo,[2,3] Ya-Jun Wang,[2,3] Ai-Yuan Hu,[1] Hiroki Saito,[4,*] Chao-Qing Dai,[5,†] and Xiao-Fei Zhang[2,3,‡]

[1]*College of Physics and Electronic Engineering, Chongqing Normal University, Chongqing 401331, China*

[2]*Key Laboratory of Time and Frequency Primary Standards, National Time Service Center, Chinese Academy of Sciences, Xi'an 710600, China*

[3]*School of Astronomy and Space Science, University of Chinese Academy of Sciences, Beijing 100049, China*

[4]*Department of Engineering Science, University of Electro-Communications, Tokyo 182-8585, Japan*

[5]*School of Sciences, Zhejiang A&F University, Lin'an, Zhejiang 311300, China*

(Received 11 July 2019; revised manuscript received 21 January 2020; accepted 20 February 2020; published 13 March 2020)

The effects of atom numbers on the miscibility-immiscibility transition of a harmonically trapped population imbalanced binary Bose-Einstein condensate are investigated. In two-dimensional parameter space expanded by the strength of interspecies interaction and the ratio of atom numbers between two components, we have mapped out the ground-state phase diagrams for the ideal model without intraspecies interactions, and for the ^{23}Na - ^{23}Na mixture and the ^{87}Rb - ^{87}Rb mixture with experimentally accessible intraspecies scattering lengths, respectively. It is found that all the phase diagrams include the miscible, symmetric immiscible, and asymmetric immiscible phases, and there exists a tricritical point where those three different phases merge. Furthermore, the phase boundaries among those three phases show a strong dependence on the atom numbers of two components. These results can be observed in current experiments.

DOI: 10.1103/PhysRevA.101.033610

I. INTRODUCTION

The experimental realization of a binary Bose-Einstein condensate (BEC) has provided a platform to investigate the novel and interesting physics in the interacting quantum gases [1–15], such as dark-bright solitons [16–23], spin drag phenomena [24], exotic vortex lattice structure [25–33], and self-bound quantum droplets [34–38], which do not exist in a single BEC. A typical feature is that the binary BEC exhibits miscible or immiscible phenomena depending on the atomic interactions. As observed in experiments [9–15], when the interspecies repulsive interaction is large enough, the two components repel each other so that they separate into two distinct clouds with small spatial overlap, corresponding to the immiscible phase. When the effect of interspecies interactions is weak compared to the intraspecies interactions, the two components are miscible and overlap with each other at the center of the trapping potential.

As is well known for a homogeneous binary BEC, where the kinetic energy is negligible compared with the interaction energy, the transition between miscible-immiscible phases can be determined only by the interspecies and intraspecies interactions. A traditional criterion for the immiscible ground state is $a_{11}a_{22} < a_{12}^2$ [39–45], where a_{11} and a_{22} are the intraspecies s-wave scattering lengths of components 1 and 2, respectively, while a_{12} is the interspecies s-wave scattering length between them. Therefore, one can control the miscibility-immiscibility transition of a binary BEC by using the Feshbach resonance technique to adjust the interaction strengths [6–8,14]. However, if a binary BEC is trapped in an inhomogeneous potential with finite size, the pressure of the trapping potential dramatically makes the binary BEC more miscible and shifts the critical value of a_{12} to a larger value for the immiscible ground state [46–48], indicating that the traditional criterion $a_{12}^2 = a_{11}a_{22}$ is not necessarily the optimal boundary of the miscible-immiscible transition for a trapped binary BEC. Furthermore, for a harmonically trapped binary BEC, it has also been confirmed that the asymmetry in atomic masses of two components also affects the boundary between miscible and immiscible phases [49–51].

In general, the immiscible case of a binary BEC exhibits two typical density profiles [9–15,41–64] (as shown in Fig. 1): (i) the symmetric immiscible phase, where one component lies at the trap center with the other lying at the periphery, and (ii) the asymmetric immiscible phase, where the two components deviate from the trap center and face one another separated by a domain wall. In particular, within the Thomas-Fermi approximation, the miscible, symmetric, and asymmetric immiscible phases can coexist at $a_{11} = a_{22} = a_{12}$ [57,58]. Although the ground-state phase diagrams of a binary BEC have been extensively studied both experimentally and theoretically, only a few studies have been focused on the effects of atom numbers and the trapping potential. Actually, in the experiment of the ^{87}Rb - ^{133}Cs mixture, McCarron *et al.* have observed that the density profiles of the ground state have

*hiroki.saito@uec.ac.jp
†dcq424@126.com
‡xfzhang@nstc.ac.cn

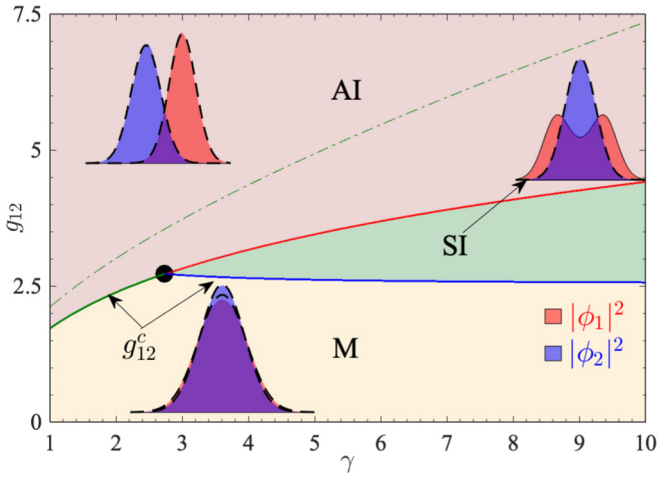

FIG. 1. The ground-state phase diagram of a binary BEC without intraspecies interactions in the g_{12}-γ plane. The red, green, and blue solid lines represent the phase boundaries given by numerical calculations, the green dot-dashed line is the critical value of g_{12} for the asymmetric immiscible ground state given by the variational method, and the solid black circle denotes the tricritical point. The insets filled by red and blue represent the density distributions of two components given by numerical calculations, and the dashed black lines in the insets of the miscible (M) and asymmetric immiscible (AI) phases are the density distributions of Gaussian variational approximation, while the dashed black line in the inset of the symmetric immiscible (SI) phase is $\phi_2 = \pi^{-1/4}e^{-z^2/2}$. The system parameters of the insets in the miscible, asymmetric immiscible, and symmetric immiscible phases are $(\gamma, g_{12}) = (2, 1)$, $(\gamma, g_{12}) = (2, 4)$, and $(\gamma, g_{12}) = (7, 3)$, respectively.

three distinct immiscible structures depending on the relative atom numbers of two species [12,62]. Very recently, Lee *et al.* have given the ground-state phase diagram of a population-imbalanced ^{87}Rb - ^{39}K mixture in the a_{11}/a_{12}-a_{12}/a_{22} plane [64], which shows that the boundaries between the miscible, asymmetric, and symmetric immiscible phases will be changed obviously for different ratios of atom numbers.

To gain more insight into the effects of the atom numbers, in this paper we consider the binary BEC with unequal atom numbers in two species, and we treat the ratio of atom numbers between two species as a continuous independent variable. For the sake of simplicity, we first consider the harmonically trapped ideal binary BEC without intraspecies interactions, which admits an analytical variational analysis and is conducive to understanding the effects of atom numbers on the immiscible-miscible transition. And then, the ^{23}Na - ^{23}Na mixture and the ^{87}Rb - ^{87}Rb mixture with experimentally accessible intraspecies scattering lengths are investigated, respectively. By using the imaginary-time propagation method to obtain the ground states for these systems, we determine the corresponding phase diagrams in two-dimensional parameter space expanded by the strength of interspecies interaction and the ratio of atom numbers between two species, which verifies again that the atom numbers of two species play an important role in the transitions among the miscible, symmetric immiscible, and asymmetric immiscible phases. For example, the critical value of interspecies interaction for the asymmetric immiscible ground state will increase monotonically with the ratio of atom numbers between two species. In particular, it has also been found that the three different phases can coexist at a tricritical point, which is related to the atom numbers of two components.

The rest of the paper is structured as follows. In Sec. II we describe the theoretical model based on mean-field theory at zero temperature. In Secs. III and IV, we will give the phase diagrams for the system with and without intraspecies interactions, respectively. Finally, we summarize these results in Sec. V.

II. THE THEORETICAL MODEL

We consider a binary BEC composed of two different hyperfine spin states of the same atom, and we assume the two species have different atom numbers, i.e., $N_1 \neq N_2$. Within the mean-field theory at zero temperature, the Gross-Pitaevskii energy functional of such a system can be written as follows [39,40]:

$$E = \int_{-\infty}^{+\infty} d^3\mathbf{r}\left\{\sum_{j=1,2}\left[\frac{\hbar^2}{2m}|\nabla\Psi_j|^2 + V(\mathbf{r})|\Psi_j|^2\right] + \frac{U_{11}}{2}|\Psi_1|^4 + \frac{U_{22}}{2}|\Psi_2|^4 + U_{12}|\Psi_1|^2|\Psi_2|^2\right\}, \quad (1)$$

where $\Psi_j(\mathbf{r})$ satisfies $\int_{-\infty}^{+\infty}|\Psi_j(\mathbf{r})|^2d^3\mathbf{r} = N_j$, with $j = 1, 2$. The trapping potential is the cylindrically symmetric harmonic potential $V(\mathbf{r}) = \frac{1}{2}m[\omega_\perp^2(x^2 + y^2) + \omega_z^2 z^2]$, where $\mathbf{r} = x, y, z$ is the spatial coordinate, m is the atom mass, and $\omega_\perp$ and ω_z are the trapping frequencies along the transverse and axial directions, respectively. The contact interaction parameters read $U_{ij} = 4\pi\hbar^2 a_{ij}/m$, with a_{ij} being the s-wave scattering length between components i and j, which can be tuned by using the Feshbach resonance [6–8,14]. In this paper, we mainly consider the repulsive atomic interactions with positive scattering lengths.

To highlight the effect of atom numbers, we set $\mathbf{r} = \xi\mathbf{r}'$ and make a transformation $\Psi_j(\mathbf{r}) = \sqrt{N_j}\xi^{-3/2}\psi_j(\mathbf{r}')$, with $\psi_j(\mathbf{r}')$ satisfying $\int_{-\infty}^{+\infty}|\psi_j(\mathbf{r}')|^2d^3\mathbf{r}' = 1$. The energy functional (1) can be rewritten in terms of the rescaled wave function $\psi_j(\mathbf{r}')$,

$$\frac{E}{E_\xi} = \int_{-\infty}^{+\infty} d^3\mathbf{r}'\left\{\sum_{j=1,2}\gamma^{j-1}\left[\frac{1}{2}|\nabla'\psi_j|^2 + V'(\mathbf{r}')|\psi_j|^2\right] + \frac{1}{2}\frac{\beta_{11}}{\gamma}|\psi_1|^4 + \frac{1}{2}\beta_{22}\gamma|\psi_2|^4 + \beta_{12}|\psi_1|^2|\psi_2|^2\right\}, \quad (2)$$

where $E_\xi = \hbar^2 N_1/(m\xi^2)$, $\beta_{ij} = N_2 m U_{ij}/(\hbar^2\xi)$, $V'(\mathbf{r}') = m^2\xi^4[\omega_\perp^2(x'^2 + y'^2) + \omega_z^2 z'^2]/(2\hbar^2)$, $\gamma = N_2/N_1$ is the ratio of atom numbers between two species, and we assume $\gamma \geqslant 1$ ($N_2 \geqslant N_1$) without loss of generality. From Eq. (2), it is obvious that the kinetic energy, the trapping potential energy, and the atomic interaction energy are all related to γ, which implies that the atom numbers will certainly affect the transitions between miscible and immiscible phases.

To investigate the effects of atom numbers on the ground state of a population-imbalanced binary BEC, we treat γ as a continuous independent variable, and we give the

ground-state phase diagram in the a_{12}-γ plane by the imaginary-time propagation method to obtain the stationary solutions of this system [65]. Since the ground-state wave functions have three different structures, we introduce the following two order parameters to distinguish these three different phases:

$$\delta = \int_{-\infty}^{+\infty} \mathbf{r}'(|\psi_1|^2 - |\psi_2|^2) d^3\mathbf{r}', \tag{3a}$$

$$\Delta_j = \frac{n_j(\mathbf{r}'=0)}{\mathrm{Max}[n_j(\mathbf{r}')]}, \tag{3b}$$

where δ represents the difference between the center of mass of two wave functions, and Δ_j is the normalized trap-center density of the jth component [64]. Consequently, the ground state is asymmetric immiscible for $\delta \neq 0$. For $\delta = 0$, $\Delta_1 = \Delta_2 = 1$ corresponds to the miscible case, and $\Delta_1 < 1$ and $\Delta_2 = 1$ (or $\Delta_1 = 1$ and $\Delta_2 < 1$) correspond to the symmetric immiscible one. In the imaginary-time propagation, different initial conditions are chosen and the propagation continues until $\mathrm{Max}[|\phi_j^{\tau_{n+1}}(\mathbf{r}') - \phi_j^{\tau_n}(\mathbf{r}')|] < e^{-10}$ and $|E(\tau_{n+1}) - E_{\tau_n}| < e^{-10}$, where τ represents the discretized imaginary time. The different types of ground states are identified by comparing the energies given by different initial conditions.

III. THE GROUND-STATE PHASE DIAGRAM OF A QUASI-ONE-DIMENSIONAL BINARY BEC WITHOUT INTRASPECIES INTERACTIONS

To gain some intuition, we first consider the quasi-one-dimensional binary BEC along the z' direction and take $a_{11} = a_{22} \equiv 0$. This ideal case not only admits a simple analytical analysis, as we shall see below, but it may also be conducive to understanding the effects of atom numbers on the immiscible-miscible transition. Therefore, we assume that the condensates are tightly confined in the $x'y'$ plane by the harmonic trap with $\omega_\perp \gg \omega_z$, and the motional degrees of freedom in the $x'y'$ plane are frozen, so that the dynamics of such a cigar-shaped binary BEC can be considered to be effectively one-dimensional along the z'-direction. In this case, we take $\xi = \sqrt{\hbar/m\omega_z}$, and we factorize the wave function as $\psi_j = \varphi_{\mathrm{ho}}(x', y')\phi_j(z')$, where $\varphi_{\mathrm{ho}}(x', y') = \sqrt{\omega_\perp/(\pi\omega_z)}\exp[-\omega_\perp(x'^2 + y'^2)/(2\omega_z)]$ is the normalized ground-state wave function of a particle trapped in a harmonic oscillator with dimensionless Hamiltonian $H = -\frac{1}{2}(\partial^2/\partial x'^2 + \partial^2/\partial y'^2) + \frac{\omega_\perp^2}{2\omega_z^2}(x'^2 + y'^2)$. By inserting the factorized wave function into the energy functional (2) and performing the integrals with respect to x' and y', we can derive the effective one-dimensional energy functional along the z' direction,

$$\frac{E}{E_\xi} = \int_{-\infty}^{+\infty} \left[\sum_{j=1,2} \frac{\gamma^{j-1}}{2}(|\partial_{z'}\phi_j|^2 + z'^2 n_j) + g_{12} n_1 n_2 \right] dz', \tag{4}$$

where the effective interspecies interaction coefficient reads $g_{12} = \xi m N_2 U_{12}/(2\pi\hbar^2\xi_\perp^2)$, and $n_j = |\phi_j|^2$ presents the density distribution of the jth component. In addition, we have omitted the constant associated with the zero-point energy of a harmonic oscillator in the x'- and y'-directions, which has no contributions to the structure of the ground state.

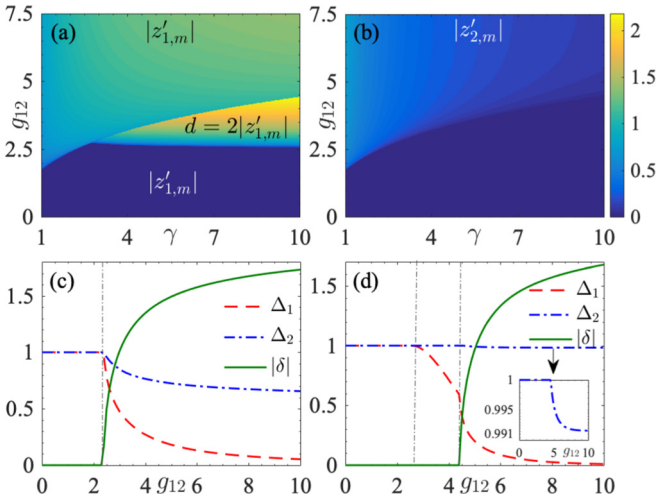

FIG. 2. Parts (a) and (b) show the locations $z'_{1,m}$ and $z'_{2,m}$ of the maximum values of two wave functions in the γ-g_{12} plane, respectively. Parts (c) and (d) show the dependencies of Δ_j and δ on g_{12} for fixed γ, where $\gamma = 2$ and 10 in (c) and (d), respectively. The vertical dot-dashed lines in (c) and (d) indicate the phase boundaries. The inset in (d) magnifies the curve of δ.

Figure 1 exhibits the ground-state phase diagram as a function of the effective interspecies interaction g_{12} and the ratio of atom numbers between two species γ, where the miscible and immiscible phases are separated by the solid green and blue lines, and we have denoted the critical value of interspecies interaction as g_{12}^c for the immiscible ground state. It is easy to see that the system is miscible for $g_{12} < g_{12}^c$, where two wave functions overlap in the center of the trap, while for $g_{12} > g_{12}^c$ the system is immiscible and exhibits two different types of density profiles: a symmetric demixed phase and an asymmetric demixed phase. In addition, we observe that both phase boundaries, for the miscible-asymmetric immiscible transition and the symmetric immiscible–asymmetric immiscible transition, increase monotonically with γ. The boundary between the miscible and symmetric immiscible ground states decreases marginally for a relatively small γ, but remains almost unchanged for a larger γ. More interestingly, there is a tricritical point at $g_{12} \simeq 2.8$ and $\gamma \simeq 2.9$ in the phase diagram, where these three different phases merge.

In Figs. 2(a) and 2(b), we have plotted the locations $|z'_{1,m}|$ and $|z'_{2,m}|$ of the maximum values of two wave functions in the g_{12}-γ plane, which also confirm the phase diagram shown in Fig. 1. In the miscible phase, the two wave functions with $z'_{1,m} = z'_{2,m} = 0$ are located at the center of the trap. In the symmetric immiscible phase, ϕ_1 forms a bilaterally symmetric structure with two identical maximum values at $z' = \pm z'_{1,m}$ to surround ϕ_2, and the distance $d = 2|z'_{1,m}|$ between the two maximum values of ϕ_1 increases with g_{12}. While g_{12} is large enough, the two wave functions separate along opposite directions and the system is in the asymmetrical immiscible phase, in which $|z'_{1,m}|$ increases but $|z'_{2,m}|$ decreases with γ for a fixed g_{12}. Moreover, for $\gamma = 2$ and 10, the dependencies of Δ_j and $|\delta|$ on g_{12} have also been shown in Figs. 2(c) and 2(d),

respectively, which show that these two order parameters changing with g_{12} are different in different phases. In the miscible phase, we have $\Delta_j = 1$ and $|\delta| = 0$, both of which will not change with g_{12}. In the asymmetric immiscible phase, $\Delta_j < 1$ and $|\delta| > 0$, the former decreases with g_{12}, while the latter increases monotonically with g_{12}. In the symmetric immiscible phase, Δ_2 and $|\delta|$ remain unchanged, but Δ_1 decreases monotonically with g_{12}, which indicates that the value of the wave function ϕ_1 at the trap center gradually reduces with increasing g_{12}.

To give a clearer understanding of the above results, we analyze the transitions among these three different phases in detail, respectively.

A. The miscible-asymmetric immiscible transition

We first focus on the miscible-asymmetric immiscible transition, where the numerical results show that far from the phase boundary, the profiles of two wave functions are similar to the Gaussian function in both miscible and asymmetric immiscible phases. Therefore, we employ the Gaussian variational method to analyze the miscible-asymmetric immiscible transition, and take the following variational wave functions [47]:

$$\phi_i = \pi^{-1/4} w_i^{-1/2} e^{[-(z'-z_i')^2/2w_i^2]}, \tag{5}$$

where w_i and z_i' are the width and center of the wave function, respectively. Inserting this ansatz into the energy function (4), we obtain

$$\frac{E_0}{E_\xi} = \frac{1}{4}\left(\frac{1}{w_1^2} + w_1^2\right) + \frac{\gamma}{4}\left(\frac{1}{w_2^2} + w_2^2\right) + \frac{1}{2}\left(z_1'^2 + \gamma z_2'^2\right) + \frac{g_{12}}{\sqrt{\pi}\sqrt{w_1^2 + w_2^2}} e^{-\frac{(z_1'-z_2')^2}{w_1^2+w_2^2}}. \tag{6}$$

Minimizing the energy (6) with respect to w_i and z_i', we can obtain

$$\frac{1}{2}\left(1 - \frac{1}{w_1^4}\right) = \frac{\left(w_1^2 + w_2^2 - 2\delta^2\right) g_{12}}{\sqrt{\pi}\left(w_1^2 + w_2^2\right)^{5/2}} e^{-\frac{\delta^2}{w_1^2+w_2^2}}, \tag{7a}$$

$$\frac{\gamma}{2}\left(1 - \frac{1}{w_2^4}\right) = \frac{\left(w_1^2 + w_2^2 - 2\delta^2\right) g_{12}}{\sqrt{\pi}\left(w_1^2 + w_2^2\right)^{5/2}} e^{-\frac{\delta^2}{w_1^2+w_2^2}}, \tag{7b}$$

$$z_1' = \frac{2 g_{12}\delta}{\sqrt{\pi}\left(w_1^2 + w_2^2\right)^{3/2}} e^{-\frac{\delta^2}{w_1^2+w_2^2}}, \tag{7c}$$

$$z_2' = -\frac{2 g_{12}\delta}{\gamma\sqrt{\pi}\left(w_1^2 + w_2^2\right)^{3/2}} e^{-\frac{\delta^2}{w_1^2+w_2^2}}, \tag{7d}$$

where $\delta = z_1' - z_2'$ corresponds to the difference between the centers of two wave functions. It can be observed that both the widths and centers of two wave functions show a strong dependence on γ.

By solving Eqs. (7), we can obtain the corresponding variational wave functions in the miscible and asymmetric immiscible phases, which agrees with the numerical results (see the insets in the miscible and asymmetric immiscible phases of Fig. 1). It is found that for both the miscible phase and the symmetric immiscible phase, the difference between the centers of two wave functions is zero. Consequently, we can obtain the critical value g_{12}^c for the onset of the asymmetric immiscible ground state by setting $\delta = 0$, that is,

$$g_{12}^c = \frac{\sqrt{\pi}}{2}\left(\frac{\gamma}{\gamma+1}\right)^{1/4}(1+\sqrt{\gamma})^{3/2}, \tag{8}$$

which illustrates that g_{12}^c increases monotonically with γ (as shown by the green dot-dashed line in Fig. 1), and it agrees qualitatively well with our numerical results. Equation (8) can also be understood from the energy (6). With increasing γ, the kinetic energy of component 2 is enhanced, which acts against the interspecies interaction. The critical value of g_{12} is therefore shifted to a large value for a larger γ as shown in Eq. (8) [46–48]. However, Eq. (8) is quantitatively different from the critical value of g_{12} given by numerical calculation (the green solid line in Fig. 1). Actually, at the beginning of asymmetric immiscible phase for $g_{12} \gtrsim g_{12}^c$, the numerical result shows that the profiles of two wave functions deviate slightly from the Gaussian function and vary slowly in space, which makes the critical value g_{12}^c always smaller than the one given by the Gaussian variational approximation. For the asymmetric immiscible phase, despite the fact that g_{12}^c in Eq. (8) deviates from the one given by numerical calculation, the analytical expression offers valuable insight into the dependence of g_{12}^c on atom numbers.

B. The miscible-symmetric immiscible transition

Next, we shift our attention to the miscible-symmetric immiscible transition. In our numerical results, for $\gamma > \gamma_{\rm tc}$, with $\gamma_{\rm tc}$ being the value at the tricritical point, when g_{12} surpasses the phase boundary denoted by the blue solid line in Fig. 1, we find that $\phi_2 \simeq \pi^{-1/4} e^{-z'^2/2}$ (see the dashed black line of the inset in the symmetric immiscible phase of Fig. 1), which is merely the ground-state wave function of a single particle in the harmonic potential. In this case, the effect of ϕ_1 on ϕ_2 via interspecies interaction can be neglected, and the effective trapping potential for ϕ_1 can be written as $z'^2/2 + g_{12} e^{-z'^2}/\sqrt{\pi}$, which acts as a barrier formed by ϕ_2 at the center of a harmonic trap with the strength proportional to g_{12}, leading to the formation of a symmetric shell structure of ϕ_1, as shown in the inset of Fig. 1. In addition, the peak of the effective potential barrier increases with g_{12}, which leads to a larger z_1' and deeper collapse of the center of ϕ_1.

Furthermore, when γ is relatively larger, the repulsive interspecies interaction is overwhelmed by the strong effective kinetic energy and trapping potential energy, and the component 2 is always in the ground state of the harmonic trapping potential. In this case, the contribution of γ to the total energy is a constant zero-point energy $\gamma/2$, and it is no use to adjust the atom numbers of two species to change the critical value of g_{12} for the miscible-symmetric immiscible transition. Therefore, the phase boundary between the miscible and symmetric immiscible phases remains almost unchanged with increasing γ. To clarify this point, we use the Gaussian variational approximation again. For the symmetric immiscible ground state, our numerical calculations show that ϕ_1 can be approximately viewed as the superposition of two Gaussian wave functions with opposite centers, that is, $\phi_1 \simeq \{\exp[-(z'-z_1')^2/(2w_1^2)] +$

$\exp[-(z'+z_1')^2/(2w_1^2)]\}/\sqrt{2\sqrt{\pi}w_1[1+\exp(-z_1'^2/w_1^2)]}$. If we take $\phi_2 = \pi^{-1/4}w_2^{-1/2}\exp(-z'^2/2w_2^2)$, then the energy functional (4) is rewritten as

$$\frac{E_0}{E_\xi} = \frac{1}{4}\left(w_1^2+\frac{1}{w_1^2}\right)+\frac{\gamma}{4}\left(w_2^2+\frac{1}{w_2^2}\right)+\frac{w_1^4 e^{z_1'^2/w_1^2}-1}{2w_1^4\left(1+e^{z_1'^2/w_1^2}\right)}z_1'^2 + \frac{e^{\frac{z_1'^2 w_2^2}{w_1^2(w_1^2+w_2^2)}}+1}{\sqrt{\pi\left(w_1^2+w_2^2\right)}\left(1+e^{z_1'^2/w_1^2}\right)}g_{12}. \quad (9)$$

Minimizing the energy (9) with respect to w_i and z_1', we find $w_2 \sim 1$ for a larger γ, as observed in the numerical calculations. In this case, the energy in Eq. (9) can be approximated as $E_0/E_\xi = \gamma/2 + f(w_1, g_{12}, z_1')$, where f is a function of the width w_1, the center z_1' of wave function ϕ_1, and the interspecies interaction g_{12}. Therefore, γ has no contributions to the width and center of ϕ_1, and the critical value g_{12}^c for the miscible-symmetric immiscible transition shows almost no dependence on γ, as confirmed by the numerical results shown in Fig. 1.

C. The symmetric immiscible-asymmetric immiscible transition

Finally, for a fixed γ with $\gamma > \gamma_{tc}$, when g_{12} further surpasses the phase boundary denoted by the red solid line in Fig. 1, the interspecies interaction will dominate the kinetic and potential energy for component 2. To minimize the interaction energy, the two components separate along opposite directions under the strong repulsive interaction, and thus the system will experience the transition from the symmetric immiscible phase to the asymmetric immiscible phase. In this transition, the concave of ϕ_1 disappears, which leads to a sudden change of Δ_1 at the boundary of the symmetric immiscible–asymmetric immiscible transition, as shown in Fig. 2(d). Moreover, as shown in the inset of Fig. 2(d), for larger γ, we have $\Delta_2 \sim 1$ and $z_2' \sim 0$ in the asymmetric immiscible phase, indicating that the component 2 with more atoms will stay almost at the center of the trap even for strong interspecies repulsive interaction, which can also be observed from Fig. 2(b).

IV. THE GROUND-STATE PHASE DIAGRAM IN THE PRESENCE OF INTRASPECIES INTERACTIONS

So far, we have focused on the ideal case without intraspecies interactions. In real experiments of a binary BEC, there are intraspecies interactions in each species. The repulsive intraspecies interactions try to expand the condensates and against the phase separation [46–48]. To see the effects of atom numbers on the miscibility-immiscibility transition in the presence of intraspecies interactions, we consider the ^{23}Na - ^{23}Na mixture and the ^{87}Rb - ^{87}Rb mixture, respectively, with experimentally realizable intraspecies scattering lengths and trap geometries, and we perform the full three-dimensional numerical calculations based on the energy functional (2) with $N_2 \equiv 10^4$ and $N_1 \in [10^3, 10^4]$ (i.e., $1 \leqslant \gamma \leqslant 10$).

We first consider the binary BEC with equal intraspecies scattering lengths, which correspond to the recent experiment on the ^{23}Na - ^{23}Na mixture [66], where the magnetic sublevels $m_F = \pm 1$ of the hyperfine spin $F = 1$ state are used for two components and the intraspecies scattering lengths are $a_{11} = a_{22} = 54.54a_B$. Moreover, to extract more underlying physics, we will also consider three different trap geometries: the spherical harmonic trap with $(\omega_\perp, \omega_z) = (10, 10)$ Hz, the oblate harmonic trap with $(\omega_\perp, \omega_z) = (10, 100)$ Hz, and the prolate harmonic trap with $(\omega_\perp, \omega_z) = (100, 10)$ Hz, which are realizable in current experiments. By using the imaginary-time propagation method to minimize the full three-dimensional energy functional (2), we depict the ground-state phase diagrams in the three different trap geometries and show the representative density profiles of two species in each phase. The results are shown in Fig. 3. As with the phase diagram of the ideal case without intraspecies interactions shown in Fig. 1, Fig. 3 shows that in the presence of equal intraspecies interactions, the phase diagrams in different trap geometries still contain three different phases, which also merge at a tricritical point. In the symmetric immiscible phase, as shown by the density profiles of two species (see the insets), the component 2 also serves as an effective potential barrier for component 1 at the harmonic trap center, leading to the formation of a symmetric shell structure in component 1. On the other hand, unlike the ideal case, due to the intraspecies interactions, the critical value of a_{12} at the boundary between the miscible and symmetric immiscible phases decreases slowly with γ, as shown by the blue lines in Fig. 3.

The tricritical point and all the phase boundaries depend quantitatively on trap geometries. If the binary BEC is trapped tightly in the transverse direction as in Fig. 3(a), we find that the energy scale of the interaction energy is much larger than that of the kinetic energy in the axial direction, and the atomic interactions always play the dominant role in determining the configuration of the ground state. Therefore, the boundary between the miscible and immiscible phases almost occurs at $a_{12}^2 \simeq a_{11}a_{22}$, and the range of the symmetric immiscible ground state in the phase diagram is very narrow, as shown in Fig. 3(a). In the oblate trap in Fig. 3(b), the atomic density is lower and the kinetic energy in the transverse direction becomes relatively important. In this case, the critical value of interspecies interaction for the immiscible ground state is shifted to a larger value [46–48], leading to a broader range of the symmetric immiscible ground state in the phase diagram as shown in Fig. 3(b). In the spherical trap in Fig. 3(c), this tendency becomes more pronounced. The tricritical point moves to smaller γ from Figs. 3(a)–3(c). Thus, the phase diagram can be controlled quantitatively by changing the trap frequencies.

Finally, we consider the asymmetric intraspecies scattering lengths (i.e., $a_{11} \neq a_{22}$), where the binary BEC is assumed to be the mixture of two internal spin states of ^{87}Rb atoms. In this case, we take, respectively, two sets of the experimentally realized intraspecies scattering lengths, one is $a_{11} = 98.98a_B$ and $a_{22} = 100.4a_B$ in the mixture of $|F = 2, m_F = 2\rangle$ and $|F = 1, m_F = 1\rangle$ hyperfine states [19], the other is $a_{11} = 95a_B$ and $a_{22} = 100.4a_B$ in the mixture of $|F = 2, m_F = -1\rangle$ and $|F = 1, m_F = 1\rangle$ hyperfine states [14]. We take the spherical harmonic trap as an example, and we consider the weak confinement with $\omega_\perp = \omega_z = 10$ Hz and the tight confinement

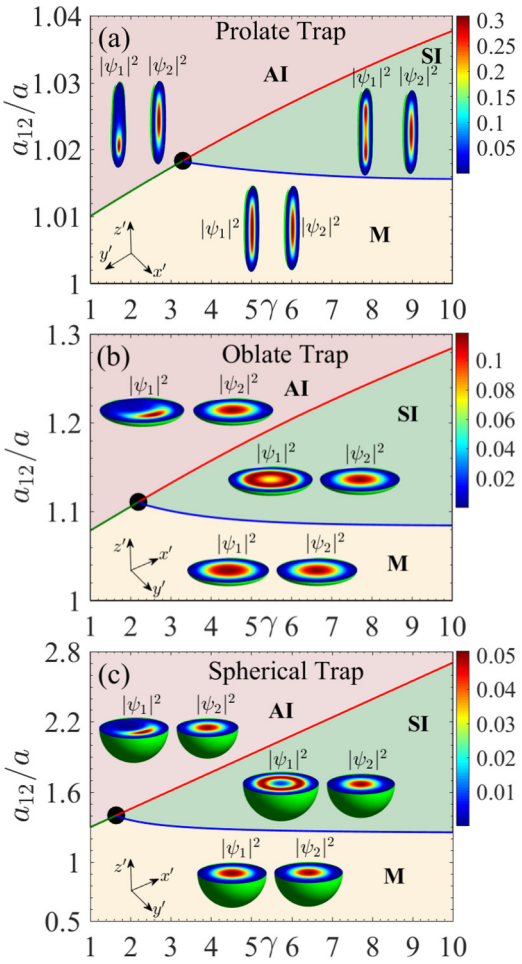

FIG. 3. The ground-state phase diagram for the ^{23}Na mixture with $a_{11} = a_{22} = a = 54.54a_B$ in different trap geometries, where the insets in each phase are the representative density profiles of two wave functions for $\gamma = 8$. The trapping frequencies are $(\omega_\perp, \omega_z) =$ (100, 10)Hz in (a), $(\omega_\perp, \omega_z) =$ (10, 100)Hz in (b), and $(\omega_\perp, \omega_z) =$ (10, 10)Hz in (c), respectively. For M, SI, and AI phases, the interspecies scattering lengths of the insets are $a_{12}/a = 1.01, 1.03, 1.04$ in (a), $a_{12}/a = 1.04, 1.2, 1.3$ in (b), and $a_{12}/a = 1.1, 2.2, 2.6$ in (c), respectively. In each inset, the green outside surface represents the isosurface of the density profile, the cross section depicts the density distribution in the $x'y'$ plane at $z' = 0$ (for the oblate and spherical traps) or in the $y'z'$ plane at $x' = 0$ (for the prolate trap), and the spatial scales in both axial and transverse directions are in $[-6\xi, 6\xi]$, where $\xi = \sqrt{\hbar/m\omega_m}$, with $\omega_m = \min\{\omega_\perp, \omega_z\}$, is the unit of space.

with $\omega_\perp = \omega_z = 100$ Hz. The ground-state phase diagrams and the representative density profiles in each phase are depicted in Fig. 4. For the case of $a_{11} = 98.98a_B$ and $a_{22} = 100.4a_B$, due to the small distinction between intraspecies scattering lengths of two species, as shown in Figs. 4(a) and 4(b), the ground-state phase diagrams in both traps are similar to the ones for $a_{11} = a_{22}$. For $a_{11} = 95a_B$ and $a_{22} = 100.4a_B$, in a relatively weak trap, the ground-state phase diagram in Fig. 4(c) is similar to Fig. 4(a). However, in a relatively strong trap, as shown in Fig. 4(d), the ground-state phase diagram has an additional symmetric immiscible phase between the miscible and asymmetric immiscible phases for $\gamma \sim 1$ (see the green area in the lower left corner of the phase

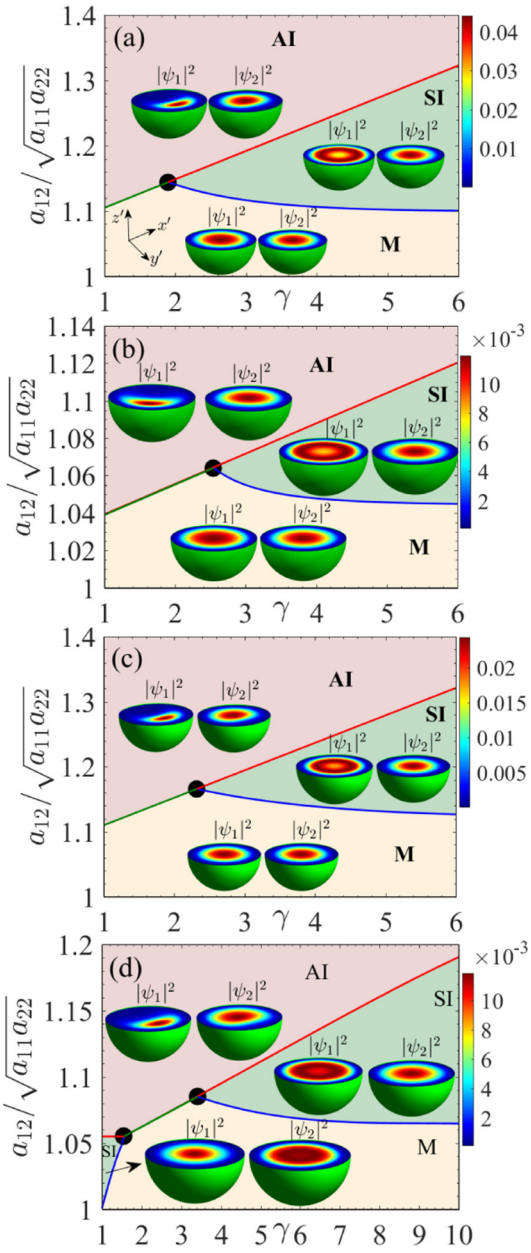

FIG. 4. The ground-state phase diagram in the $a_{12}/\sqrt{a_{11}a_{22}}$-$\gamma$ plane for the ^{87}Rb mixture with $a_{11} \neq a_{22}$, where $(a_{11}, a_{22}) =$ $(98.98, 100.4)a_B$ in (a) and (b), $(a_{11}, a_{22}) = (95, 100.4)a_B$ in (c) and (d), and the insets in each phase diagram are the representative density profiles in three different phases. The trapping frequencies are $(\omega_\perp, \omega_z) = (10, 10)$ Hz in (a) and (c), and $(\omega_\perp, \omega_z) = (100, 100)$ Hz in (b) and (d). The parameters of the insets in (a) and (c) are $\gamma = 5$ and $a_{12}/\sqrt{a_1 1 a_{22}} = 1.05, 1.25, 1.4$ for the M, SI, and AI regions, respectively. In (b), the parameters of the insets in the M, SI, and AI regions are $(\gamma, a_{12}/\sqrt{a_{11}a_{22}}) = (5, 1.02), (5, 1.08), (5, 1.14)$, respectively. In (d), the parameters of the insets in the left SI region are $\gamma = 1.1$ and $a_{12}/\sqrt{a_{11}a_{22}} = 1.04$, and the parameters of the insets in AI and the right SI regions are $(\gamma, a_{12}/\sqrt{a_{11}a_{22}}) =$ $(5, 1.08), (5, 1.14)$, respectively. In each inset, the green outside surface represents the isosurface of the density profile, the cross section depicts the density distribution in the $x'y'$ plane at $z' = 0$, and the spatial scales in both axial and transverse directions are in $[-6\xi, 6\xi]$, where $\xi = \sqrt{\hbar/m\omega_m}$ with $\omega_m = \min\{\omega_\perp, \omega_z\}$ is the unit of space.

diagram). In this symmetric immiscible phase, since the BEC is in the Thomas-Fermi regime and $a_{11} < a_{22}$, the component 2 extends outward and forms a symmetric shell to surround the component 1 for minimizing the interaction energy (see the insets). With increasing γ, the effective kinetic energy is enhanced gradually and the phase separation is suppressed. As a result, the symmetric immiscible phase is compressed gradually and finally disappears at the tricritical point. When γ is large enough, the tricritical point and symmetric immiscible phase emerge again, but the difference is that the component 1 surrounds the component 2 in this symmetric immiscible phase (see the insets), as observed before. We would like to point out that the tricritical point on the left side of Fig. 4(d) is similar to the one found by Svidzinsky *et al.* [57,58], which is caused by the asymmetric intraspecies interactions of two species in the Thomas-Fermi regime. On the other hand, the tricritical point as well as the symmetric immiscible phase on the right side of Fig. 4(d) are caused purely by the asymmetry in atom numbers of two species, as analyzed in the case without intraspecies interactions.

V. CONCLUSION

We have studied the ground-state structures of a population-imbalanced binary BEC in a harmonic potential. In the two-dimensional parameter space expanded by the interspecies interaction and the ratio of atom numbers of two components, for the binary BEC without intraspecies scattering lengths and the ^{23}Na - ^{23}Na or ^{87}Rb - ^{87}Rb mixtures with experimentally realizable intraspecies scattering lengths, we have mapped out the corresponding ground-state phase diagrams, which are composed of three different configurations: the miscible ground state where two wave functions overlap at the center of trap, the symmetric immiscible ground state where one component forms a shell structure around the other, and the asymmetric immiscible ground state where the two wave functions separate along opposite directions. It is verified that the phase boundaries among these three different configurations depend strongly on the atom numbers of two components; there exist tricritical points in the phase diagram, where those three different phases merge. The parameters used in this work are within current experimental capacity.

ACKNOWLEDGMENTS

We are grateful to An-Chun Ji and Qing Sun for helpful discussions. This work is supported by NSFC under Grants No. 11875010, No. 11504037, and No. 11775253; by the Natural Science Foundation of Chongqing under Grant No. cstc2019jcyj-msxmX0217; by the Key Research Program of Frontier Sciences, CAS, Grant No. ZDBS-LY-7016; by the Youth Innovation Promotion Association of CAS under Grant No. 2015334; and by the JSPS KAKENHI Grants No. JP17K05595 and No. JP17K05596.

[1] G. Modugno, M. Modugno, F. Riboli, G. Roati, and M. Inguscio, Two Atomic Species Superfluid, Phys. Rev. Lett. **89**, 190404 (2002).

[2] M. Mudrich, S. Kraft, K. Singer, R. Grimm, A. Mosk, and M. Weidemüller, Sympathetic Cooling with Two Atomic Species in an Optical Trap, Phys. Rev. Lett. **88**, 253001 (2002).

[3] S. Sugawa, R. Yamazaki, S. Taie, and Y. Takahashi, Bose-Einstein condensate in gases of rare atomic species, Phys. Rev. A **84**, 011610(R) (2011).

[4] P. Maddaloni, M. Modugno, C. Fort, F. Minardi, and M. Inguscio, Collective Oscillations of Two Colliding Bose-Einstein Condensates, Phys. Rev. Lett. **85**, 2413 (2000).

[5] A. D. Lercher, T. Takekoshi, M. Debatin, B. Schuster, R. Rameshan, F. Ferlaino, R. Grimm, H.-C. Nägerl, Production of a dual-species Bose-Einstein condensate of Rb and Cs atoms, Eur. Phys. J. D **65**, 3 (2011).

[6] S. B. Papp, J. M. Pino, and C. E. Wieman, Tunable Miscibility in a Dual-Species Bose-Einstein Condensate, Phys. Rev. Lett. **101**, 040402 (2008).

[7] G. Thalhammer, G. Barontini, L. De Sarlo, J. Catani, F. Minardi, and M. Inguscio, Double Species Bose-Einstein Condensate with Tunable Interspecies Interactions, Phys. Rev. Lett. **100**, 210402 (2008).

[8] L. Wacker, N. B. Jørgensen, D. Birkmose, R. Horchani, W. Ertmer, C. Klempt, N. Winter, J. Sherson, and J. J. Arlt, Tunable dual-species Bose-Einstein condensates of ^{39}K and ^{87}Rb, Phys. Rev. A **92**, 053602 (2015).

[9] C. J. Myatt, E. A. Burt, R. W. Ghrist, E. A. Cornell, and C. E. Wieman, Production of Two Overlapping Bose-Einstein Condensates by Sympathetic Cooling, Phys. Rev. Lett. **78**, 586 (1997).

[10] D. S. Hall, M. R. Matthews, J. R. Ensher, C. E. Wieman, and E. A. Cornell, Dynamics of Component Separation in a Binary Mixture of Bose-Einstein Condensates, Phys. Rev. Lett. **81**, 1539 (1998).

[11] K. L. Lee, N. B. Jørgensen, L. J. Wacker, M. G. Skou, K. T. Skalmstang, J. J. Arlt and N. P. Proukakis, Time-of-flight expansion of binary Bose-Einstein condensates at finite temperature, New J. Phys. **20**, 053004 (2018).

[12] D. J. McCarron, H. W. Cho, D. L. Jenkin, M. P. Köppinger, and S. L. Cornish, Dual-species Bose-Einstein condensate of ^{87}Rb and ^{133}Cs, Phys. Rev. A **84**, 011603(R) (2011).

[13] B. Pasquiou, A. Bayerle, S. M. Tzanova, S. Stellmer, J. Szczepkowski, M. Parigger, R. Grimm, and F. Schreck, Quantum degenerate mixtures of strontium and rubidium atoms, Phys. Rev. A **88**, 023601 (2013).

[14] S. Tojo, Y. Taguchi, Y. Masuyama, T. Hayashi, H. Saito, and T. Hirano, Controlling phase separation of binary Bose-Einstein condensates via mixed-spin-channel Feshbach resonance, Phys. Rev. A **82**, 033609 (2010).

[15] F. Wang, X. Li, D. Xiong, and D. Wang, A double species ^{23}Na and ^{87}Rb Bose-Einstein condensate with tunable miscibility via an interspecies Feshbach resonance, J. Phys. B **49**, 015302 (2016).

[16] C. Becker, S. Stellmer, P. Soltan-Panahi, S. Dorscher, M. Baumert, E.-M. Richter, J. Kronjager, K. Bongs, and K. Sengstock, Oscillations and interactions of dark and dark-bright solitons in Bose-Einstein condensates, Nat. Phys. **4**, 496 (2008).

[17] Th. Busch and J. R. Anglin, Dark-Bright Solitons in Inhomogeneous Bose-Einstein Condensates, Phys. Rev. Lett. **87**, 010401 (2001).

[18] V. Achilleos, D. Yan, P. G. Kevrekidis, and D. J. Frantzeskakis, Dark-bright solitons in Bose-Einstein condensates at finite temperatures, New J. Phys. **14**, 055006 (2012).

[19] C. Hamner, J. J. Chang, P. Engels, and M. A. Hoefer, Generation of Dark-Bright Soliton Trains in Superfluid-Superfluid Counterflow, Phys. Rev. Lett. **106**, 065302 (2011).

[20] S. Rajendran, P. Muruganandam, and M. Lakshmanan, Interaction of dark-bright solitons in two-component Bose-Einstein condensates, J. Phys. B **42**, 145307 (2009).

[21] X.-F. Zhang, X.-H. Hu, X.-X. Liu, and W. M. Liu, Vector solitons in two-component Bose-Einstein condensates with tunable interactions and harmonic potential, Phys. Rev. A **79**, 033630 (2009).

[22] M. A. Hoefer, J. J. Chang, C. Hamner, and P. Engels, Dark-dark solitons and modulational instability in miscible two-component Bose-Einstein condensates, Phys. Rev. A **84**, 041605 (2011).

[23] M. O. D. Alotaibi and L. D. Carr, Dynamics of dark-bright vector solitons in Bose-Einstein condensates, Phys. Rev. A **96**, 013601 (2017).

[24] S. B. Koller, A. Groot, P. C. Bons, R. A. Duine, H. T. C. Stoof, and P. van der Straten, Quantum enhancement of spin drag in a Bose gas, New J. Phys. **17**, 113026 (2015).

[25] E. J. Mueller and T.-L. Ho, Two-Component Bose-Einstein Condensates with a Large Number of Vortices, Phys. Rev. Lett. **88**, 180403 (2002).

[26] K. Kasamatsu, M. Tsubota, and M. Ueda, Vortex Phase Diagram in Rotating Two-Component Bose-Einstein Condensates, Phys. Rev. Lett. **91**, 150406 (2003).

[27] R. Barnett, G. Refael, M. A Porter, and H. P. Buchler, Vortex lattice locking in rotating two-component Bose-Einstein condensates, New J. Phys. **10**, 043030 (2008).

[28] P. Mason and A. Aftalion, Classification of the ground states and topological defects in a rotating two component Bose-Einstein condensate, Phys. Rev. A **84**, 033611 (2011).

[29] C.-H. Hsueh, T.-L. Horng, S.-C. Gou, and W. C. Wu, Equilibrium vortex formation in ultrarapidly rotating two-component Bose-Einstein condensates, Phys. Rev. A **84**, 023610 (2011).

[30] R. Wei and E. Mueller, Vortex structures of a two-component Bose-Einstein condensate for large anisotropies, Phys. Rev. A **84**, 063611 (2011).

[31] A. Aftalion, P. Mason, and J. Wei, Vortex-peak interaction and lattice shape in rotating two-component Bose-Einstein condensates, Phys. Rev. A **85**, 033614 (2012).

[32] P. Kuopanportti, J. A. M. Huhtamäki, and M. Möttönen, Exotic vortex lattices in two-species Bose-Einstein condensates, Phys. Rev. A **85**, 043613 (2012).

[33] K. Kasamatsu and M. Tsubota, Vortex sheet in rotating two-component Bose-Einstein condensates, Phys. Rev. A **79**, 023606 (2009).

[34] D. S. Petrov, Quantum Mechanical Stabilization of a Collapsing Bose-Bose Mixture, Phys. Rev. Lett. **115**, 155302 (2015).

[35] C. R. Cabrera, L. Tanzi, J. Sanz, B. Naylor, P. Thomas, P. Cheiney, L. Tarruell, Quantum liquid droplets in a mixture of Bose-Einstein condensates, Science **359**, 301 (2018).

[36] P. Cheiney, C. R. Cabrera, J. Sanz, B. Naylor, L. Tanzi, and L. Tarruell, Bright Soliton to Quantum Droplet Transition in a Mixture of Bose-Einstein Condensates, Phys. Rev. Lett. **120**, 135301 (2018).

[37] V. Cikojević, K. Dželalija, P. Stipanović, and L. V. Markić, Ultradilute quantum liquid drops, Phys. Rev. B **97**, 140502(R) (2018).

[38] G. Semeghini, G. Ferioli, L. Masi, C. Mazzinghi, L. Wolswijk, F. Minardi, M. Modugno, G. Modugno, M. Inguscio, and M. Fattori, Self-Bound Quantum Droplets of Atomic Mixtures in Free Space, Phys. Rev. Lett. **120**, 235301 (2018).

[39] C. J. Pethick and H. Smith, *Bose-Einstein Condensation in Dilute Gases* (Cambridge University Press, Cambridge, 2002).

[40] L. Pitaevskii and S. Stringari, *Bose-Einstein Condensation* (Oxford University Press, New York, 2003).

[41] T.-L. Ho and V. B. Shenoy, Binary Mixtures of Bose Condensates of Alkali Atoms, Phys. Rev. Lett. **77**, 3276 (1996).

[42] P. Ao and S. T. Chui, Binary Bose-Einstein condensate mixtures in weakly and strongly segregated phases, Phys. Rev. A **58**, 4836 (1998).

[43] H. Pu and N. P. Bigelow, Properties of Two-Species Bose Condensates, Phys. Rev. Lett. **80**, 1130 (1998).

[44] E. Timmermans, Phase Separation of Bose-Einstein Condensates, Phys. Rev. Lett. **81**, 5718 (1998).

[45] P. Öhberg, Stability properties of the two-component Bose-Einstein condensate, Phys. Rev. A **59**, 634 (1999).

[46] L. Wen, W. M. Liu, Y. Cai, J. M. Zhang, and J. P. Hu, Controlling phase separation of a two-component Bose-Einstein condensate by confinement, Phys. Rev. A **85**, 043602 (2012).

[47] R. Navarro, R. Carretero-Gonzalez, and P. G. Kevrekidis, Phase separation and dynamics of two-component Bose-Einstein condensates, Phys. Rev. A **80**, 023613 (2009).

[48] R. N. Bisset, P. G. Kevrekidis, and C. Ticknor, Enhanced quantum spin fluctuations in a binary Bose-Einstein condensate, Phys. Rev. A **97**, 023602 (2018).

[49] B. Tanatar and K. Erkan, Strongly interacting one-dimensional Bose-Einstein condensates in harmonic traps, Phys. Rev. A **62**, 053601 (2000).

[50] H. Ma and T. Pang, Condensate-profile asymmetry of a boson mixture in a disk-shaped harmonic trap, Phys. Rev. A **70**, 063606 (2004)

[51] V. Cikojević, L. V. Markić, and J. Boronat, Harmonically trapped Bose-Bose mixtures: a quantum Monte Carlo study, New J. Phys. **20**, 085002 (2018).

[52] S. T. Chui and P. Ao, Broken cylindrical symmetry in binary mixtures of Bose-Einstein condensates, Phys. Rev. A **59**, 1473 (1998).

[53] H. Shi, W. M. Zheng, and S. T. Chui, Phase separation of Bose gases at finite temperature, Phys. Rev. A **61**, 063613 (2000).

[54] M. Trippenbach, K. Góral, K. Rzazewski, B. Malomed, and Y. B. Band, Structure of binary Bose-Einstein condensates, J. Phys. B **33**, 4017 (2000).

[55] F. Riboli and M. Modugno, Topology of the ground state of two interacting Bose-Einstein condensates, Phys. Rev. A **65**, 063614 (2002).

[56] J. G. Kim and E. K. Lee, Characteristic features of symmetry breaking in two-component Bose-Einstein condensates, Phys. Rev. E **65**, 066201 (2002).

[57] A. A. Svidzinsky and S. T. Chui, Symmetric-asymmetric transition in mixtures of Bose-Einstein condensates, Phys. Rev. A **67**, 053608 (2003).

[58] A. A. Svidzinsky and S. T. Chui, Normal modes and stability of phase-separated trapped Bose-Einstein condensates, Phys. Rev. A **68**, 013612 (2003).

[59] S. Ronen, J. L. Bohn, L. E. Halmo and M. Edwards, Dynamical pattern formation during growth of a dual-species Bose-Einstein condensate, Phys. Rev. A **78**, 053613 (2008).

[60] D. H. Santamore and E. Timmermans, Spin critical opalescence in zero-temperature Bose-Einstein condensates, Europhys. Lett. **97**, 36009 (2012).

[61] I. Vidanović, N. J. van Druten, and M. Haque, Spin modulation instabilities and phase separation dynamics in trapped two-component Bose condensates, New J. Phys. **15**, 035008 (2013).

[62] R. W. Pattinson, T. P. Billam, S. A. Gardiner, D. J. McCarron, H. W. Cho, S. L. Cornish, N. G. Parker, and N. P. Proukakis, Equilibrium solutions for immiscible two-species Bose-Einstein condensates in perturbed harmonic traps, Phys. Rev. A **87**, 013625 (2013).

[63] I.-K. Liu, R. W. Pattinson, T. P. Billam, S. A. Gardiner, S. L. Cornish, T.-M. Huang, W.-W. Lin, S.-C. Gou, N. G. Parker, and N. P. Proukakis, Stochastic growth dynamics and composite defects in quenched immiscible binary condensates, Phys. Rev. A **93**, 023628 (2016).

[64] K. L. Lee, N. B. Jørgensen, I.-K. Liu, L. Wacker, J. J. Arlt, and N. P. Proukakis, Phase separation and dynamics of two-component Bose-Einstein condensates, Phys. Rev. A **94**, 013602 (2016).

[65] W. Bao and Y. Cai, Mathematical models and numerical methods for spinor Bose-Einstein condensates, Commun. Comput. Phys. **24**, 899 (2018).

[66] E. Fava, T. Bienaim, C. Mordini, G. Colzi, C. Qu, S. Stringari, G. Lamporesi, and G. Ferrari, Observation of Spin Superfluidity in a Bose Gas Mixture, Phys. Rev. Lett. **120**, 170401 (2018).